Nanomed. J. 8(1): 42-56, Winter 2021

RESEARCH PAPER

Probing the effects of synthesized silver nanowire/reduced graphene oxide composites on the structure and esterase-like activity of human serum albumin and its impacts on human endometrial stem cells: A new platform in nanomedicine

Azadeh Hekmat [1*], Shadie Hatamie [2,3], Elham Bakhshi [1]

[1]Department of Biology, Science and Research Branch, Islamic Azad University, Tehran, Iran
[2]Institute of NanoEngineering and MicroSystems, National Tsing Hua University, Hsinchu 30013, Taiwan
[3]Department of Power Mechanical Engineering, National Tsing Hua University, Hsinchu 30013, Taiwan

ABSTRACT

Objective(s): Nowadays, the unique and fascinating properties of graphene-based nanocomposites make them one of the most promising materials for therapeutics, delivery carriers as well as tissue engineering. On the other hand, silver nanowire has been attracting more attention in nanomedicine applications, too. In this study, the effects of synthesized silver nanowire/reduced graphene oxide (AgNWs/rGO) composites on the structure and esterase-like activity of Human Serum Albumin (HSA), as well as its impacts on Human Endometrial Stem Cells (hEnSCs), were evaluated

Materials and Methods: AgNWs/rGO composite was first synthesized and fabricated. Subsequently, its effects on the structure and esterase-like activity of HSA were evaluated by UV-Visible spectroscopy, circular dichroism spectroscopy, and fluorescence spectroscopy. Afterward, its impacts on the viability and growth of hEnSCs were studied by MTT assay, DAPI staining, and flow cytometry analysis.

Results: The spectroscopic results showed that AgNWs/rGO composite could form a complex with HSA, however, did not affect the secondary structure of HSA and the binding constant for this complex was found to be 5.4×104 mL.mg-1. Furthermore, HSA maintained most of its activity in the presence of the AgNWs/rGO composite. Based on FRET (fluorescence resonance energy transfer) data the value of r0 was less than 7 nm signifying that the energy transfer from HSA to AgNWs/rGO composite occurs with a high level of possibility. The MTT assay, DAPI staining, and flow cytometry analysis indicated that the AgNWs/rGO composite was non-toxic towards hEnSCs.

Conclusion: Our results suggest that the prepared AgNWs/rGO composite, potentially, is suitable in nanomedicine applications such as tissue engineering and drug delivery.

Keywords: *Esterase-Like Activity, Human Endometrial Stem Cells, Human Serum Albumin (HSA),Silver nanowire/reduced graphene oxide, Zeta Potential*

How to cite this article

Hekmat A, Hatamie Sh, Bakhshi E. Probing the effects of synthesized Silver nanowire/reduced graphene oxide composites on the structure and esterase-like activity of human Serum albumin and its impacts on human endometrial stem cells: A new platform in Nanomedicine. Nanomed J. 2021; 8(1): 42-56. DOI: 10.22038/nmj.2021.08.05

INTRODUCTION

Graphene (one of the carbon crystalline forms) is single-monolayer carbon atoms strongly packed into a two-dimensional (2D) honeycomb lattice. Each carbon atom of graphene has one out-of-plane π-bond and three σ-bonds that can interact with neighboring atoms [1, 2]. Due to its electron distribution and atomic structure, graphene has glamorous physicochemical properties such as a large surface area (about 2600 m2.g-1), best thermal, mechanical, and electrical properties, distinctive optical behaviors, as well as excellent chemical stability.

Thru physicochemical modifications, graphene sheets can be converted into graphene-related materials with unique properties for example graphene oxide (GO) and reduced graphene oxide (rGO) [3]. Since 2004, these kinds of materials have attracted interest in the field of biomedicine such

* *Corresponding Author Email: : hekmat@ut.ac.ir*
Note. This manuscript was submitted on September 3, 2020; approved on November 20, 2020

as cancer therapy, drug delivery, photothermal therapy, regenerative medicine, gene transfection, antibacterial activity, several biological imaging modalities, and also tissue engineering [1, 3-7]. However, the genotoxicity and cytotoxicity of graphene, even at low concentration (10 µg/mL), have been shown. Consequently, further treatments and attentions are required in bio-applications of graphene which normally require high concentrations of graphene (>10 µg/mL). It has been verified that functionalized graphene could induce lower cytotoxic effects [8, 9]. It has been shown that graphene and GO can interact with biomolecules for instance proteins, DNA, peptides, and enzymes [1, 10, 11].

Nano-silver, as one of the most valuable nanomaterials, has been applied in the bio-nanotechnology industry extensively with a focus on its antibacterial, antifungal, antiviral, and especially antitumor activity [12]. Nano-silver materials can synthesize in various shapes such as silver nanowires (AgNWs), silver nanocubes (AgNCs), silver nanoparticles (AgNPs), and silver nanorods (AgNRs). Nanowires are one type of one-dimensional (1D) nanomaterials. Currently, 1D nanostructures have attracted a lot of attention, and scientists have discovered innovative procedures for producing nanowires [13]. Nowadays, AgNWs have also been utilized in nanomedicine and nanobiotechnology including drug delivery, biomarker detection, wearable devices, biosensors, and biomimetic scaffolds [14].

Human serum albumin (HSA) is a helical triple-domain structure protein contains 585 amino acids in its single polypeptide chain [15]. The study of the interaction between nanomaterial and HSA has been a great area of research in chemical biology and pharmacology. Binding of nanomaterial to HSA results in increased nanomaterial solubility in plasma as well as decreased toxicity. This binding can affect the distribution and elimination of nanomaterial [16]. However, binding of the nanomaterial with HSA could alter the intramolecular forces that are responsible for stabilizing the HSA conformation. Consequently, the investigation of the binding induced structural variations in the secondary and tertiary structure of HSA *in vitro* upon interaction with nanomaterial remains important in terms of verifying the biocompatibility of nanomaterial *in vivo* [17].

Stem cells are characterized by their capacity to initiate tissue-specific committed progenitors or differentiated cells or proliferate indefinitely (self-renewal). The human endometrium is a very dynamic tissue, which undergoes cycles of regression and growth with each menstrual cycle. The human endometrial stem cells (hEnSCs) can expand rapidly without leading to major technical and ethical issues and also can generate a higher overall clonogenicity, thus, they have unique potential as autologous therapeutic agents [18, 19].

As mention earlier, the unique and fascinating properties of graphene-based nanocomposites make them one of the most promising materials for therapeutics, delivery carriers as well as tissue engineering. Even though numerous challenging issues remain, the biomedical applications of graphene-based nanocomposites have noteworthy potential. Consequently, in this article, at first, silver nanowire/reduced graphene oxide composite (AgNWs/rGO composite) was synthesized and characterized. Then, the probable effects of the prepared AgNWs/rGO composite on HSA structure and its esterase-like activity in physicochemical terms were evaluated. Afterward, the impacts of AgNWs/rGO composite on the growth and viability of hEnSCs were investigated. The findings obtained from this investigation can provide useful information for the wide application of AgNWs/rGO composite in the nanomedical field especially tissue engineering and drug delivery.

MATERIALS AND METHODS

Materials

Graphite powder, sulfuric acid, purified sodium nitrite (NaNO3), purified potassium permanganate (KMnO4), hydrogen peroxide (H2O2 30%), hydrochloric acid, purified silver nitrate (AgNO3), ethylene glycol (EG), platinum chloride, polyvinylpyrrolidone (PVP; MW=55000), acetone, ethanol, methanol, and sodium nitrite were acquired from Merck Co. (Germany). Human Serum Albumin (lyophilized powder, essentially fatty acid-free), hydrazine hydrate (N2H4), Tris(hydroxymethyl) aminomethane (Tris-base), *p*-nitrophenyl acetate (*p*-NPA), DAPI (4'-6-Diamidino-2-phenylindole), and MTT (3-[4, 5-dimethylthiazol-2-yl]-2, 5-diphenyl tetrazolium bromide) were acquired from Sigma Aldrich Co. (USA). The cell culture medium (DMEM), penicillin fetal bovine serum (FBS), streptomycin, and Trypsin-EDTA were supplied by Gibco (USA). The Annexin FITC Kit was acquired from the IQ

product (Netherlands).

Instruments

The Barnstead™ Nanopure infinity water purification system (USA), the Varian Cary 100 Bio UV-Visible Spectrophotometer (Agilent Technologies, USA), the FTIR spectrometer (NEXUS 870, Thermo Nicolet; the Thermo Fisher Scientific, USA), the AVIV 215 Circular Dichroism Spectrometer (Aviv Biomedicals Inc., USA), the scanning electron microscope (SEM; Zeiss DSM 960A, Carl Zeiss, Germany), the transmission electron microscopy (TEM; Philips EM-208, Netherlands), the XRD (Seifert 3003 T/T, Seifert, Germany), the Zeta-Potential (Zetasizer Nano-ZS, Malvern Instruments Ltd, UK), the ELISA reader (Model Expert 96, Asys HitChech, Austria), the Flow cytometry (Partec PAS III, Parted, Germany), the fluorescence microscope (Axoscope 2 plus, Zeiss, Germany), and the Cary Eclipse fluorescence spectrophotometer (Agilent Technologies, USA) were applied.

Synthesis of reduced graphene oxide (rGO)

At first, GO was synthesized chemically by utilizing a modified Hummers' method [2, 7]. Briefly, 0.5 g of graphite powder was dispersed in 23 mL sulfuric acid (H2SO4) and kept at an ice bath (below 0°C temperatures) and stirred for 10 min. Subsequently, 0.5 g of sodium nitrite (NaNO3) was added to the acidic graphite dispersion with continuous stirring (below 0 °C temperatures). After 2 hr, 3 g of KMnO4 was added to the suspension very slowly and the reaction was continued by stirring the solution at 0 °C. After 10 min, the ice bath was removed, then the temperature of the reaction was incremented to 35°C. Subsequently, the mixture was stirred for 4 hr. Then, the mixture was diluted with slow addition of deionized water (100 mL). The solution was stirred for 30 min and subsequently, the reaction temperature was incremented rapidly to 98 °C. At this step, the mixture color changed to brown color. By adding 3 mL of H2O2 and 50 mL of deionized water, the reaction was completed, and the color of the solution changed to yellow color. For purification, the as-made GO was washed once utilizing hydrochloric acid (HCl) diluted through water and centrifuged. The final washing was performed by deionized water numerous times until the pH of GO solution reached 7. After washing, the exfoliation process was performed utilizing ultra-sonication (120 W) for 1 h. Finally, the as-synthesized GO was dried in an oven at 50 °C for 24 hr. The GO was obtained as a powder. For the synthesis of rGO, 0.5 ml N2H4 was added to 0.1 wt.% GO aqueous solution (50 ml). The mixture was then stirred for 24 h in a water bath of 95°C. Black precipitates appeared through the reduction. By vacuum filtration, the rGO product was collected and desiccated with the freeze-drier for 48h.

Synthesis of silver nanowire (AgNWs)

AgNWs were synthesized consistent with slight modifications to the solvothermal procedure [20]. At first, PVP (3.1 g) and NaCl (32 mg) were dissolved in 28 mL of EG. Then, 0.5 g of AgNO3 was dissolved in 42 mL of EG in dark. Subsequently, the reaction solution of PVP/EG/NaCl was injected into the AgNO3/EG solution drop by drop under vigorous stirring. The mixture solution was then kept at 120 for 10 min and transferred to the Teflon-lined autoclave and kept at 160 for 7 hr. Finally, the autoclave was cooled down to room temperature. The reaction products were washed with ethanol and the mixture was centrifuged at 2000 rpm for 20 min. This centrifugation procedure was repeated many times till the supernatant became colorless and NWs samples free of smaller particles were acquired. The stock suspension of AgNWs was stored at 4 in dark for further characterizations.

Synthesis of silver nanowire/reduced graphene oxide composite (AgNWs/rGO composite)

The AgNWs/rGO composite was synthesized using the hydrothermal method [7, 21]. At first, 35 mg of as made rGO was dispersed in 20 mL of deionized water and stirred until the mixture became homogeneous. After that, the mixture solution was sonicated for 1 hr. Afterward, in separate flasks, 10 mg of as-made AgNWs was dispersed in 20 mL deionized water and stirred until the solution became homogeneous. To facilitate the AgNWs/rGO composite assembly process, the AgNWs solution was added dropwise to the rGO solution and stirred for 2 hr to complete mixing. Next, the mixture was sonicated for about 20 min. Afterward, the final product was transferred to a Teflon-lined autoclave then heated at 180 °C for 18 hr. To remove unreacted components, the black precipitation was washed 5 times through ethanol. Later, the product was poured into the plate and dried at 50°C in an oven for 24 h. Finally,

the AgNWs/rGO composite powder was collected and stored for further characterizations.

Nanomaterial characterization

rGO, AgNWs, and AgNWs/rGO composite powder were used to take X-ray diffraction (XRD). The XRD patterns were obtained using Cu Kα radiation of a wavelength of 0.154 nm. By employing the Scherrer equation (Eq. 1), the crystal size (*D*) of nanomaterials was calculated [22]. In this equation, λ, β and ϑ are the wavelength of the X-rays in nanometer (nm), the peak full width of the diffraction peak profile at half-maximum height (in radians), and the scattering angle in radians, respectively.

$$D = \frac{0.9\lambda}{\beta \cos\theta} \quad (1)$$

Fourier transform infrared (FTIR) spectra in the range of 400-4000 cm-1 and Ultraviolet-Visible (UV-Vis) spectra in the range of 230-500 nm of rGO, AgNWs, and AgNWs/rGO composite were acquired by FTIR and UV-Vis spectrometer, respectively. The surface morphology of rGO, AgNWs, and AgNWs/rGO composite was analyzed by scanning electron microscope (SEM). The average diameter of the nanomaterials was statistically calculated utilizing a computed image analyzer (ImageJ) by measuring 25 distinct points at random. The diameters were presented as the average ± standard deviation. The morphology of as-synthesized samples was characterized by utilizing a transmission electron microscope (TEM). Samples were made by drying a droplet of nanomaterial suspension on a carbon-coated copper grid.

Steady-state fluorescence measurements

Steady-state fluorescence emission spectra of HSA (15.0 µM) after addition of AgNWs/rGO composite (10-55 mg/mL) were explored. The width of the slits for excitation and emission were 10 nm and 10 nm, respectively. The experiments were done in a quartz cell (1 cm path length). The excitation and emission wavelengths were 280 nm and 348 nm, respectively. For inner filter effect correction caused by the attenuation of the signals of the excitation and emission produced from the quencher absorption, Eq. 2 was used [15].

$$F_{corr} = F_{obs}.10^{(Ab_{ex}+Ab_{em})/2} \quad (2)$$

In equation 2, *Fcorr*, *Fobs*, *Abex*, and *Abem* are the corrected intensities, the observed fluorescence intensities, the mixture absorption at excitation, and the mixture absorption at emission wavelengths, respectively. All trials were performed in a Tris-based buffer (0.1 M, pH 7.4).

Ultraviolet-visible (UV-Vis) measurements

The UV–Vis spectra of 15.0 µM solution of HSA after the addition of diverse amounts of AgNWs/rGO composite (10-55 mg/mL) were recorded at 37 °C. All experiments were run and verified in Tris-based buffer (0.1 M, pH 7.4) in a 1 cm quartz cell.

Circular dichroism (CD) measurements

The far-UV CD spectra of 15.0 µM solution of HSA in the absence and presence of AgNWs/rGO composite (55 mg/mL) were recorded from 190 to 260 nm. The experiments were done in a quartz cell (0.1 cm path length).The speed of scanning was 20 nm min-1 and the resolution was 0.2 nm. Thru subtracting the proper baseline, each CD spectra were corrected. Experiments were performed in a Tris-based buffer (0.1 M, pH 7.4) at 37 ºC. The CD spectra deconvolution software (CDNN; version 2.1) was utilized to deconvolute all CD spectra based on the spectra ranging from 190 to 260 nm.

Zeta potential measurements

The zeta (*z*) potential of HSA (15.0 µM), AgNWs/rGO composite (55 mg/mL) and HSA-AgNWs/rGO composite were measured. The test suspension was diluted with deionized water. Results from five experiments were averaged.

Esterase-Like activity assay

The impact of AgNWs/rGO composite on the esterase-like activity of HSA was investigated with the synthetic substrate *p*-NPA (*p*-nitrophenyl acetate). HSA upon interacting with *p*-NPA released *p*-nitrophenyl. The reaction mixture contained 50 µM *p*-NPA, 15 µM of HSA solution, and 55 mg.mL-1 AgNWs/rGO composite. The absorbance of the released *p*-nitrophenyl was recorded at 400 nm using a UV-Vis spectrophotometer. The molar extinction coefficient (ε) was taken as 17700 M−1 cm−1 to analyze the concentration of *p*-nitrophenol [23]. One unit of esterase activity was defined as the amount of enzyme required to release 1 µM of *p*-nitrophenol per min at 37 °C.

Cells and cell culture

The human endometrial stem cells (hEnSCs) were a kind gift from professor J. Ai [18, 19].

The hEnSCs were maintained in DMEM medium accompanied by penicillin and streptomycin (1%), and heat inactivated FBS (10%) in a 5% CO2 humidified atmosphere incubator at 37 °C. Every three days, the medium was changed and passage three were utilized for the experiments.

Cell viability and proliferation assay

The MTT reduction assay was utilized to measure the cellular metabolic activity of hEnSCs in the presence of AgNWs/rGO composite [18]. The hEnSCs were collected with trypsin-EDTA (0.05%) once 90% of confluence was reached in T25 flasks. Subsequently, the hEnSCs were washed with PBS buffer then 1×104 cells were seeded into each well of 96-well plates at a growth medium of 170 µL and left to attach to the plates. Later, the hEnSCs incubated with numerous concentrations of the sterilized AgNWs/rGO composite (10, 30, 50, 70, 90, and 110 µg/mL). After 48 h of incubation, the medium of all wells was replaced by a fresh medium. Afterward, 20 µL MTT (5 mg/mL in PBS buffer) was added into all wells and incubated for 4 h at 37 °C. Subsequently, the insoluble formazan formed was dissolved in DMSO (100 µl). The OD (optical density) of all wells, which was considered as a function of the concentration of converted dye, was verified at a wavelength of 570 nm employing an ELISA reader.

Flow cytometry analyses

The hEnSCs were plated into 24-well plates at a density of 106 cells/well and left to attach to the plates. Subsequently, cells were incubated with 70 and 110 µg/mL of the sterilized AgNWs/rGO composite. After 48 h, the cells were collected through centrifugation at 1000g for 5 min and washed by PBS twice, and suspended in 100 µL of Annexin V binding buffer. Consequently, the hEnSCs were double-stained with 10 µL FITC-labeled Annexin V and 10 µL PI (Propidium iodide) solution (50 µg/mL in PBS). The samples were incubated at room temperature in the darkness for 20 min, subsequently investigated through flow cytometry.

DAPI staining

Approximately 1×105 cells/well were seeded in 24-well plates and incubated with sterilized AgNWs/rGO composite (70 and 110 µg/mL) for a time course of 48 h. The hEnSCs were washed with cold PBS and adjusted to a cell density of 1×106 utilizing PBS. DAPI solution (1 mg/mL in double-distilled H2O) was added to the cell suspension at a final concentration of 100 µg/mL. Then, the cellular morphology was visualized through a fluorescence microscope.

Statistical analysis

The data are recorded as mean ± standard deviation of the mean (n=3). A one-way analysis of variance (ANOVA) was utilized to compare the mean of different data sets, and the value of $P \leq 0.05$ was considered as statistically significant.

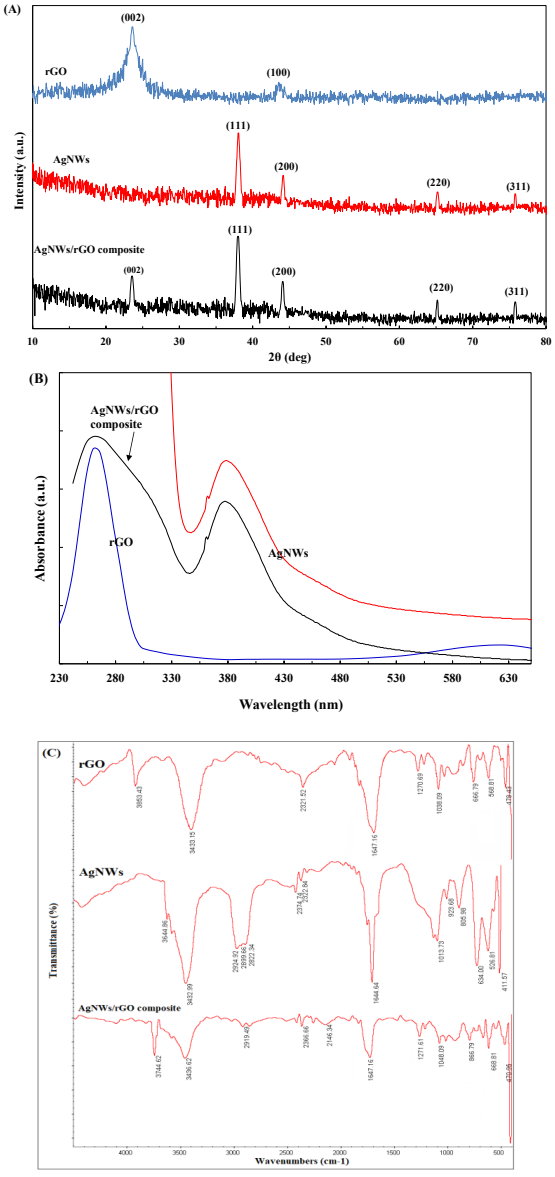

Fig 1. X-ray diffraction patterns (A); UV-Vis spectra (B); and FTIR spectra (C) of rGO, AgNWs, and AgNWs/rGO composite

RESULTS AND DISCUSSION

Characterization of nanomaterials

X-ray diffraction (XRD) is the most applied technique for the characterization of crystalline material. Fig 1A demonstrates a sharp peak at 2θ~23.9° (with inter planner distance of 3.72 Å) and a small peak at 2θ~43.8°, relating to the (002) and (100) planes of the rGO structure, respectively (ICDD No: 75-1621). No diffraction peak at 2θ~11° can be detected, signifying a complete reduction of GO to rGO [2]. Fig. 1A demonstrates diffraction peaks of AgNWs at 2θ~38.4°, 44.7°, 64.2°, and 77.8°, corresponding to the crystallographic planes of (111), (200), (220), and (311) of the face-center-cubic Ag, respectively (ICDD No: 04-0783). This observation is consistent with those of Roy *et al*. [2]. The determined inter planner distance for peaks (111), (200), (220), and (311) were 2.36 Å, 2.03 Å, 1.45 Å, and 1.23 Å, respectively. By using the Scherrer equation (Eq. 1) the AgNWs crystal size was estimated to be~50 nm in the (111) direction and 47 nm in the (200) direction. No other peaks can be detected, proving a high purity of the prepared AgNWs. Additionally, sharp and strong peaks indicated that the prepared AgNWs possess an excellent crystalline degree. As seen in Fig. 1A, AgNWs/rGO composite has a diffraction peak of both rGO and AgNWs. The diffraction peaks at 2θ~38.4° (111), 44.7° (200), 64.2° (220), and 77.8° (311) belong to crystalline Ag and the diffraction peaks at 2θ~23.9° (002) and 43.8° (100) belong to rGO. No diffraction peaks for any other impurities were detected. A peak at 38.4° is a distinctive peak for the Ag metal, which indicates that the Ag is present on the surface of rGO. This result coincided with that reported by Roy *et al*. [2]. The diffraction peak intensity of rGO at 2θ~23.9° was observed to be decreased, which confirmed that the AgNWs were well dispersed and were attached to the layers of the rGO surface. Applying Eq. 1, the mean crystallite size of the AgNWs/rGO composite was calculated to be 30 nm in the (111) direction.

The UV-Vis spectra of rGO, AgNWs, and AgNWs/rGO composite are shown in Fig. 1B. The prepared rGO possesses an absorption peak at around 265 nm. According to the literature, GO exhibited an absorption peak at 230 nm (due to the aromatic C–C ring transition) and a weak broad absorption peak at a wavelength 300 nm (due to the C=O bonds transition) [2]. Thus, the presence of the absorption peak at around 265 nm and the absence of an absorption peak at 300 nm in as-synthesized rGO can be due to the reduction in oxygen functional groups [2]. The UV–Visible absorption spectrum of as-synthesized AgNWs in deionized water exhibited two absorption peaks, at around 350 nm and 380 nm. The peak at 350 nm is due to the longitudinal mode of AgNWs or attributable to the out-of-plane quadrupole mode of AgNWs. The absorption peak at around 380 nm corresponds to the AgNWs transverse plasmon resonance [24]. The AgNWs/rGO composite exhibited noteworthy adsorption peaks centering at around 265 nm, 350 nm, and 380 nm which were characteristic peaks of rGO and AgNWs, respectively. This observation is consistent with those of Tran *et al.* [24].

Fourier transform infrared spectroscopy (FTIR) was employed to clarify the functional groups of rGO, AgNWs, and AgNWs/rGO composite (Fig. 1C). The C–O stretching vibration of the alkoxy group (1038 cm−1), a very weak C–O stretching (1270 cm−1), and C=C stretching vibration of aromatic groups (1647 cm−1) were detected in the FTIR spectra of as-made rGO. The absence of carbonyl and carboxylic acid C=O stretching vibration (1733 cm−1) specified the negligible amount of oxidation in the rGO sample [2]. In the FT-IR spectrum of the as-made AgNWs, the presence of a peak at the wavenumber of 3432 cm-1 is associated with the OH groups of solvents. The presence of peaks at 2924 cm-1 and 2822 cm-1 corresponding to the symmetric and asymmetric stretching vibration of CH2 in the PVP chain, respectively. The peak at 2899 cm-1 is related to the asymmetric stretching vibration of CH2 in the heterocyclic ring of PVP. The peak at the wavenumber of 1644 cm-1 is related to the C=O stretching vibration of PVP. These peaks in the FTIR spectrum of AgNWs signify the traces of PVP remaining in the as-made AgNWs [25]. A very weak C–O stretching (1270 cm−1), C–O stretching vibration of alkoxy group (1048 cm−1), C=C stretching vibration of aromatic groups (1647 cm−1), and O–H stretching vibration (3433 cm−1) were distinguished in the FTIR spectra of AgNWs/rGO composite [2]. However, there is a considerable reduction in the intensity of the absorption bands of the functional groups which can be probably attributable to the existence of AgNWs on the rGO surface.

Scanning Electron microscopy (SEM) imaging of as-synthesized rGO exhibited a degree of agglomeration of graphene layers (Fig 2A).

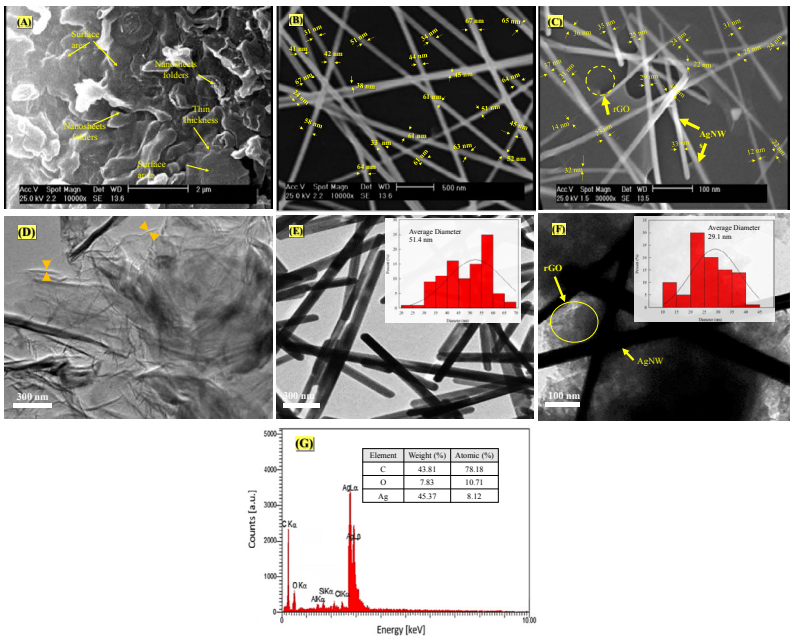

Fig 2. SEM images of rGO (A), AgNWs (B), and AgNWs/rGO composite (C); TEM images and the corresponding particle size distribution histograms of rGO (D), AgNWs (E), and AgNWs/rGO composite (F); EDX images of AgNWs/rGO composite from SEM (G)

Agglomeration happened because rGO sheets tend to aggregate during the drying of dispersion. There were also some folds on the surface of rGO sheets which could have been produced during the sample preparation. These observations were similar to the results found by Yousef *et al*. [26]. Fig 2B exhibited the SEM image of AgNWs, demonstrating a structure of AgNWs. It can be seen in Fig 2C that the AgNWs/rGO composite was formed and the surface of rGO was decorated with AgNWs. It can be seen that AgNWs prevented the agglomeration of rGO lamellae, which demonstrated a good interfacial interaction between the AgNWs and rGO.

A TEM image of rGO exposes the folded structure (Fig 2D). The TEM image of the as-synthesized AgNWs exhibits a uniform structure (Fig 2E). The as-synthesized AgNWs has an average diameter of 51 nm, which is in good consistency with XRD data. TEM image of AgNWs/rGO composite displays that AgNWs (with an average size of 29.1 nm) adsorbed and dispersed uniformly on each side of the rGO sheets (Fig 2F). It can be detected that the average diameter of AgNWs in AgNWs/rGO composite significantly decreased compared with that of pure AgNWs. To determine the weight and atomic percentage of elemental components of AgNWs/rGO composite, EDX analysis was performed (Fig 2G). As shown in the EDX spectra of AgNWs/rGO composite C, Ag, and O are the major elements in the as-synthetized composite (44 wt.% C, 8 wt.% O, and 45 wt.% Ag). A peak near 1.0 keV was detected, which corresponds to C, and a peak around 3 keV was associated with the binding energy of AgL.

Steady-State fluorescence studies

One of the most effective techniques to explore protein folding and protein-ligand interaction is fluorescence spectroscopy [27]. Commonly, the intrinsic fluorescence of HSA is obtained by the lone Trp (Tryptophan) residue of HSA which is located at position 214 (the Trp 214 residue) [28]. Any alterations in polarity around the Trp 214 residue (fluorophore) could be evaluated by the shift in the fluorescence emission peak (λmax,em) [27]. As shown in Fig 3A, HSA has an obvious and strong λmax,em at around 349 nm after being excited with a wavelength of 285 nm, however, AgNWs/rGO composite has almost no fluorescence intensity in its free form in solution. The titration of the AgNWs/rGO composite initiated a reduction in the fluorescence intensity of HSA with no shift. This phenomenon points out the formation of a complex between AgNWs/rGO composite and HSA [29]. Our data correlated well with those of Nan *et al.* [30] who have established that no shifted in the λmax,em of BSA after the addition of

GO revealed that the polarity around Trp 214 was not changed. This result is also in agreement with the conclusion derived from BSA and rGO-silver nanoparticles composite fluorescence quenching data [31]. The comparison of the present result with prior observations [20, 29-31] leads to the following conclusion: the interaction between AgNWs/rGO composite and HSA could induce minor conformational modifications with limited effects on HSA structure. A reduction (quenching) in the λmax,em of HSA also indicated that the AgNWs/rGO composite could bind near the Trp 214 amino acid residue [32].

Determination of quenching mechanism

Any process that initiates a reduction in the fluorescence emission peak could be considered as quenching which could occur by several molecular mechanisms, for example, energy transfer, molecular rearrangement, ground-state complex formation (static quenching), and collisional (dynamic) quenching [30, 33]. Hence, the classical Stern-Volmer equation (Eq. 3) was utilized to realize the mechanisms involved in the quenching phenomenon [31, 34]:

$$\frac{F_0}{F} = 1 + K_{sv}[Q] \quad (3)$$

Where *F*, *F*0, and [Q] are the fluorescence data in the presence of AgNWs/rGO composite, fluorescence data in the absence of AgNWs/rGO composite, and the concentration of quencher (AgNWs/rGO composite), respectively. *KSV* is the Stern-Volmer dynamic quenching value constant [33, 34]. Applying Eq. 3, the plot for *F0/F* vs. [AgNWs/rGO composite] was drawn (inset of Fig 3B).

As illustrated, the experimental Stern-Volmer plot for AgNWs/rGO composite displayed a positive deviation. Accordingly, the mechanism of binding of AgNWs/rGO composite to HSA commenced mainly through the formation of the non-fluorescence complex (static quenching) [35]. This data correlated well with those of Nan *et al.* [30] who have determined that the quenching mechanism of GO-BSA principally occurred through static quenching.

Determination of binding parameters

The *KA* (the binding constant) and *n* (the number of binding sites) were determined for HSA-AgNWs/rGO composite. Presuming that there were independent and equivalent binding groups in HSA, along with Eq. 4, *KA* and *n* were calculated [36].

$$\log\frac{F_0 - F}{F} = \log K_A + n\log[\mathrm{Q}] \quad (4)$$

Consistent with Fig 3B the values of *KA* and *n* for HSA-AgNWs/rGO composite were attained. The plot presented a good linear relationship. Consistent with Fig. 3B, we calculated *KA* = 5.4×104 mL.mg-1 and *n* = 0.9. The value of *n* was nearly equal to 1 suggesting that AgNWs/rGO composite could bind to HSA, forming a 1:1 adduct. This data correlated well with those of Nan *et al.* [30] and Zhang *et al.* [31] who have confirmed a single binding site existence in BSA through interacting with GO and rGO-silver nanoparticles, respectively. It is important to mention that *KA* value is commonly expressed in M-1 unit. However, because the exact molecular weight of AgNWs/rGO composite cannot be determined, in this work, we expressed its value in mL.mg-1 unit.

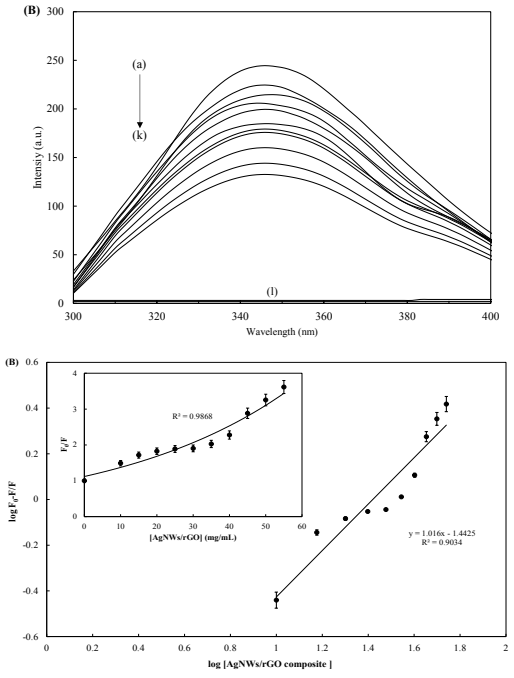

Fig 3.The fluorescence emission spectra of HSA after adding various concentrations of AgNWs/rGO composite (A). The fluorescence emission of free HSA (a), the fluorescence quenching with increasing concentrations of nanomaterial (b-k), and the fluorescence of AgNWs/rGO composite alone (l). The Modified Stern-Volmer plot of HSA in the presence of diverse concentrations of AgNWs/rGO composite (B). The Inset indicates the classic Stern–Volmer plot of HSA in the presence of diverse concentrations of AgNWs/rGO composite. The data are obtained from the Means of three independent measurements ± SD

Fluorescence resonance energy transfer (FRET) Studies

FRET has been utilized as a "spectroscopic ruler" for analysis of the distance (*r*) between the acceptor (ligand) and the donor (Trp residues in the protein). By utilizing FRET, the distance between AgNWs/rGO composite and HSA can be estimated [32]. Along with the Förster theory, the distance of binding between AgNWs/rGO composite and HSA and the efficiency (*E*) of the energy transfer between the donor (HSA) and the acceptor (AgNWs/rGO composite) can be calculated by Eq. 5 [30].

$$E = 1 - \frac{F}{F_0} = \frac{R_0^6}{R_0^6 + r_0^6} \quad (5)$$

Where *R*0 is the critical distance when the transfer efficiency between the acceptor and donor is 50% [32].

$$R_0^6 = 8.79 \times 10^{-25} k^2 N^{-4} \Phi J \quad (6)$$

In Eq. 6, *K*2 and *N* are the dipole special orientation factor and the refracted index of the medium, respectively [32]. Moreover, *Φ* and *J* are the HSA fluorescence quantum yield and the integral overlap area between the HSA emission spectrum (the donor) and the absorption spectrum of AgNWs/rGO composite (the acceptor), respectively. *J* can be calculated according to Eq. 7 [32].

$$J = \sum F(\lambda)\varepsilon(\lambda)\lambda^4 / \sum F(\lambda)\Delta\lambda$$

Where *ε*(*λ*) and *F*(*λ*) are the extinction coefficient of AgNWs/rGO composite at wavelength *λ* and the corrected fluorescence intensity of HSA in the wavelength range *λ* to *λ*+Δ*λ*, respectively [32].

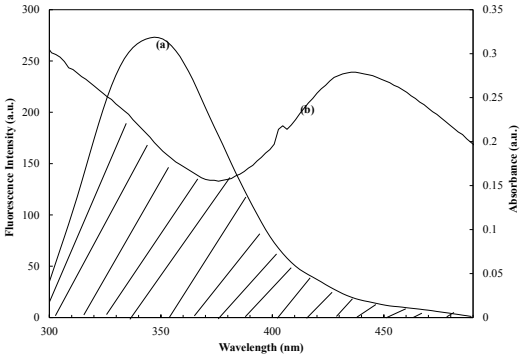

Fig 4. Spectral overlap of an absorption spectrum of AgNWs/rGO composite (a) with fluorescence emission spectrum of HSA (b)

The overlap of fluorescence spectra of HSA (15.0 µM) and the UV absorption spectra of AgNWs/rGO composite (55 mg/mL) is displayed in Fig 4. There was a good overlapping between the fluorescence emission spectrum of HSA and the absorption spectra of AgNWs/rGO composite. In the present case, applying *K*2 = 2/3, *N* = 1.336, and *Φ* = 0.12 as well as applying Eqs. (5)-(7), we calculated *R*0 = 7.8 nm, *E* = 0.7, and *r0* = 6.8 nm. The value of *r0* is less than 7 nm signifying that the energy transfer from HSA to AgNWs/rGO composite occurs with a high level of possibility [32]. This data described the efficient quenching of the HSA fluorescence in the presence of AgNWs/rGO composite.

UV absorption measurements

To provide information for the structural effect of AgNWs/rGO composite on HSA, the UV absorption spectra of HSA in the absence and presence of nanocomposite were acquired. As illustrated in Fig 5, HSA has two strong absorption bands (*λ*max): ~220 nm and around 280 nm. The absorption band at around 220 nm assigned to the $\pi \rightarrow \pi^*$ transition of $C=O$ in the HSA backbone [34, 36]. The *λ*max at approximately 280 nm in the HSA spectrum is attributed to the $\pi \rightarrow \pi^*$ transition of phenyl rings in Trp, Tyr (Tyrosine) as well as Phe (phenylalanine) [36].

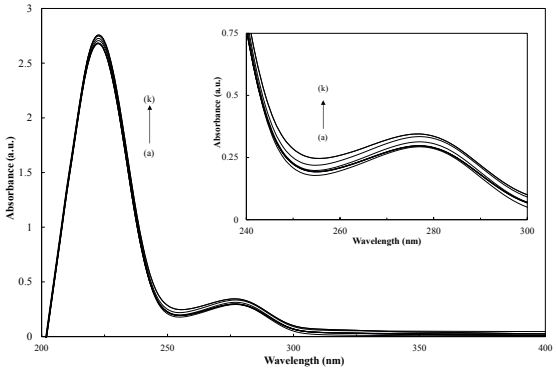

Fig 5. The UV-Visible spectra of HSA (a) with increasing concentrations of AgNWs/rGO composite (b-k). The inset illustrates the alterations in HSA maximum absorbance (280 nm) in the presence of various AgNWs/rGO composite in the wavelength range of 240 to 300 nm

The *λ*max at 280 nm is dependent on the micro-environment of the aromatic residues [36]. Besides, the *λmax* at 220 nm signifies the HSA framework structure. As realized in Fig 5, after the addition of AgNWs/rGO composite the absorption intensity of HSA increased at 220 nm and 280 nm, which demonstrated minor structural variations in the micro-environment around the amide bonds of HSA.

There is no red shift or blue shift in the *λmax* at 280 nm, indicating that the reaction between AgNWs/rGO composite and HSA is a noncovalent interaction in nature [27]. Additionally, the AgNWs/rGO composite generated a slight redshift in the *λmax* near 220nm (from 220 nm to 223 nm). According to the literature, the λmax near 220 nm is initiated by the electron displacement transition of peptide bonds, it is also correlated with the spiral content of the α-helix structure of the protein [36]. Thus, an increment in the HSA spectra after the addition of AgNWs/rGO composite revealed that AgNWs/rGO composite was a favor for the union within and between the HSA molecules, and subsequently, the configuration of HSA altered. This alternation could induce the intramolecular effect as well as the α-helix quantity reduction [36]. When AgNWs/rGO composite was added into the HSA solution, fewer HSA molecules were attached to AgNWs/rGO composite. The HSA further denatured, and the main chain uncurled causing more probability to encounter H2O, particularly for the amide moieties that used to be in the hydrophobic pocket of HSA, i.e. the HSA peptide strands were loosened partly and the aromatic amino acids were subjected to a more hydrophilic area [34, 36]. Thus, the $\delta \rightarrow \delta^*$ electronic transition energy gap was reduced, and the probability of electronic transition was incremented [36].

According to literature, in collisional quenching, no difference in the maximum absorption peak could be detected. However, an alteration in the intensity of λmax could be distinguished in the static quenching process [37]. The maximum absorption peaks of HSA were changed by adding diverse concentrations of AgNWs/rGO composite (Fig 5). This further confirmed the static quenching mechanism.

Table 1. Content of the secondary structure of 15 µM HSA in the absence and presence of AgNWs/rGO composite at 37 ºC

	α-Helix (%)[a]	β-Sheet (%)[b]	Random coil (%)[c]
HSA	52.87	22.14	24.97
HSA-AgNWs/rGO composite	45.01	24.96	30.00

Circular dichroism (CD) spectroscopic studies

The secondary structure of a protein is very sensitive to its environment. The CD spectra can be utilized extensively to study how secondary structure varies with environmental conditions [38]. As exhibited in Fig 6, two negative bands ~208 nm and ~222 nm were detected in the far-UV CD spectrum of free HSA. The far-UV CD spectrum for all α-helical protein has two double minimum around 208 nm (for π→ π* transition) and 222 nm (for n→ π* transition) as well as a strong maximum around 191-193 nm (for π→π* transition) [39]. The energy and intensity of these transitions are related to the peptide bond angles (Ψ and Φ), and therefore the protein secondary structure. As shown in Table 1, free HSA consists of 52.87% α-helix, 23.14% β-sheet, and 23.97% random coil. Hence, our result demonstrated that HSA has an α-helical structure. This finding has been confirmed by other groups [27, 38].

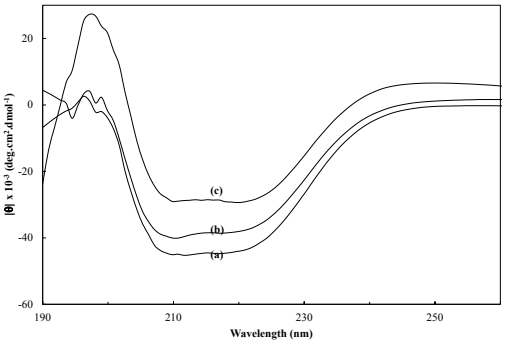

Fig 6.The far-UV CD spectra of HSA in the absence (a) and presence of AgNWs/rGO composite (b)

From Fig 6 and Table 1, the addition of AgNWs/rGO composite to HSA solution caused a slight reduction in the ellipticity of HSA, which expressed that the α-helical content of HSA reduced. Wang *et. al.* [27] and Fu *et. al.* [40] stated that when the ellipticity of HSA diminishes moderately, demonstrating some loss of α-helical secondary structure. Our data correlated well with those of Zhao *et al.* [34] who have established a diminution in the α-helical structure f BSA and an increase in the β-sheet structure of BSA after the addition of carbon nanotubes. Corrêa and Ramos [39] published that the band at around 222 nm is associated with the hydrogen-bonding environment of the α-helical secondary structure. Consequently, based on these publications we could deduce that due to the fact that the HSA ellipticity diminished partially after the addition of AgNWs/rGO composite, this nanomaterial could eliminate the hydrogen-bonding networks of HSA slightly. Importantly, the loss of α-helical content revealed that AgNWs/rGO composite binding could cause a little unfolding in the polypeptides of HSA, i.e., HSA preserves its secondary structure

and helicity when interact with AgNWs/rGO composite [40].

Zeta potential studies

The charge density or zeta (ζ) potential is a particle's surface electrical charge measurement [41]. The ζ-potential of HSA in the absence and presence of nanocomposite were examined. The ζ-potential of free HSA was found to be -16.9±0.6 mV. This data is compatible with former observations [20, 42]. HSA is a 66 kDa protein with 585 amino acidic residues, isoelectric point (pI) 4.7, and 17 disulfide bridges. At neutral pH (7.4), HSA possesses regions that are strongly negatively charged even though it has positively charged pockets, too. The three domains of HSA contain net charges of -9 mv, -8 mv, and +2 mv (for domains I, II, as well as III, respectively) [42]. The ζ-potential magnitude of AgNWs/rGO composite in buffer was found to be -25.7±0.3 mV. This data is compatible with former observation [2]. After the addition of AgNWs/rGO composite to HSA, the surface charge was decreased to -12.7±0.6 mV. As mention above, at pH 7.4 the amphiphilic HSA is negatively charged, however, there are lots of positively charged Lys residues on the HSA surface. Roy *et al.*

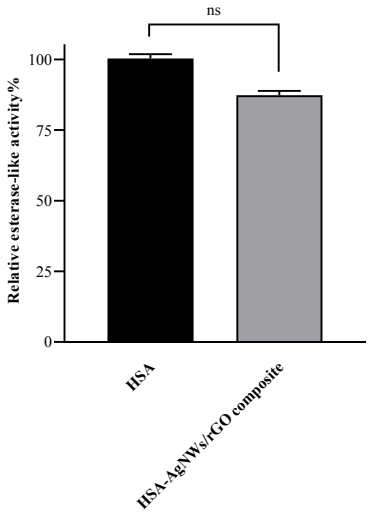

Fig 7. Effect of AgNWs/rGO composite on the activity of HSA (ns = non-significant)

[2] displayed that BSA could adsorb onto rGO through hydrophobic interactions and π-π stacking. Furthermore, previous observation displayed that the positively charged domain of BSA could interact with negatively charged surfaces of citrate-coated gold NPs or silica [43]. Consequently, HSA could interact with AgNWs/rGO composite through specific chemical bonding between HSA and AgNWs owing to the presence of imidazole, thiol, and amine groups in HSA (i.e., His, Cys, and Lys, residues).

Additionally, π-π stacking and hydrophobic interactions could play important functions in this interaction.

Analysis of the esterase-like activity of HSA

As mention earlier, our data showed that HSA maintains its secondary structure and its helicity when interacting with the AgNWs/rGO composite. It has been published that two amino acid residues (Arg410 and Tyr411) of HSA situated in site II (subdomain IIIA) display catalytic cleavage mechanisms and contributed to the esterase-like activity of HSA [23]. As shown in Fig 7, HSA maintained 87% of its original activity in the presence of AgNWs/rGO composite.

Growth rates of human endometrial stem cell

As shown in Fig. 8A, AgNWs/rGO composite did not have any negative effects on the proliferation rate of hEnSCs. However, at higher concentrations (>110 µg/mL) of AgNWs/rGO composite, some toxic effects (~25 −30% cell destruction) were detected. This result correlated well with those of Hatamie *et. al.* [8] who have shown that curcumin-rGO could not induce apoptosis in mouse fibroblast L929 cell line at concentrations lower than 70 µg.mL-1.

It has been also shown that rGO makes obvious cytotoxic effects in cells [8]. Consequently, the slight cytotoxic effects of AgNWs/rGO composite could be attributable to the presence of the AgNWs on the surface of rGO. The presence of AgNWs on the surface of rGO prevented aggregation of the reduced sheets as well as enhanced the effective thickness of the sheets.

Morphological studies

It is accepted that the blue fluorescent DAPI marker binds with Adenine-Thymine groups in the minor groove of double-strand DNA. Binding of DAPI with double-strand DNA produces approximately 20-fold fluorescence enhancement. As shown in Fig 8B, the viable hEnSCs were uniformly blue. No significant differences were observed between the hEnSCs treated with AgNWs/rGO composite (70 µg/mL) and the control

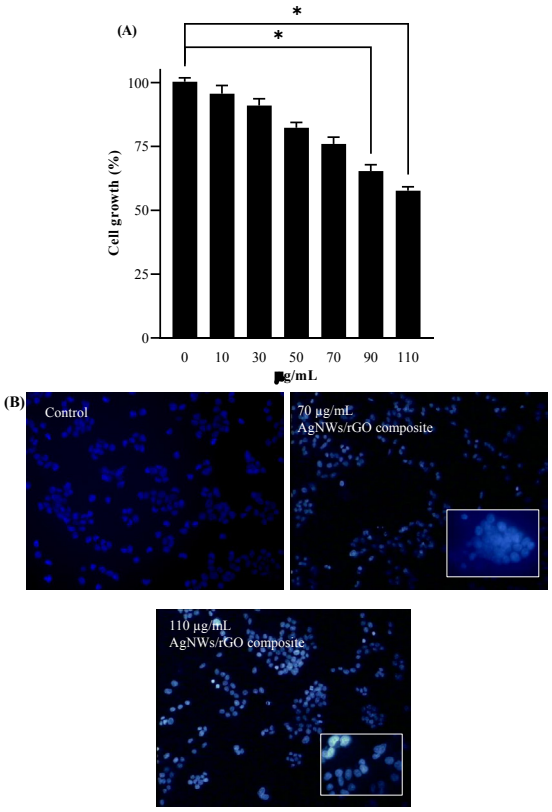

Fig 8. The effects of AgNWs/rGO composite at varying concentrations on the hEnSCs growth (A). *P < 0.05 compared to untreated control cells. Fluorescence microscopic images of hEnSCs in the absence and presence of AgNWs/rGO composite (B). The cells were stained with DAPI

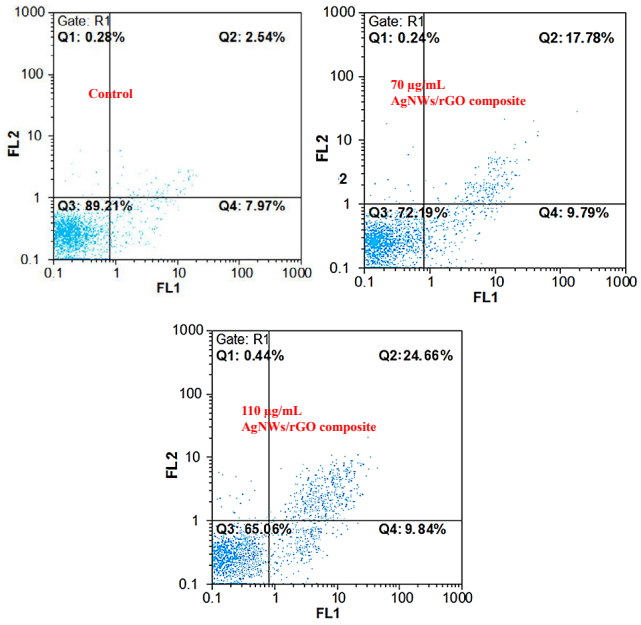

Fig 9. Dot plots of PI vs. Annexin V staining followed by flow cytometry analyses for hEnSCs in the absence and presence of AgNWs/rGO composite

group, which indicates that this nanocomposite has no toxic effects on the viability of the cells. However, at higher concentrations of AgNWs/rGO composite (>110 µg.mL-1) slight cytotoxic effects of AgNWs/rGO composite could be observed. This result is in agreement with the MTT assay experiment as mention above.

Flow cytometry analysis

To approve that there was no incident of major under- or overestimation of cell death, the values of necrotic and apoptotic cells were measured by analyzing membrane integrity and phosphatidylserine externalization through flow cytometry [12]. The flow cytometry results are shown in Fig 9. Results exhibited that the value of the living cells did not decrease after the treatment of hEnSCs with AgNWs/rGO composite (70 µg/mL). However, at a higher concentration of AgNWs/rGO composite (110 µg/mL), the value of the living cells decreased slightly. Furthermore, the percentage of apoptotic cells increased at a higher concentration of AgNWs/rGO composite. Consequently, AgNWs/rGO composite was non-toxic towards the hEnSCs at lower concentrations. Based on our MTT assay, flow cytometry analysis, and previous publications [8, 44-46], the slight cytotoxic effects of AgNWs/rGO composite could be attributable to the presence of AgNWs on the surface of rGO which prevented aggregation of rGO sheets. These results revealed that the functionalized-rGO nanocomposite (here, AgNWs/rGO composite) can efficiently be utilized in nanotechnology-based bio-applications that required high concentrations of graphene, without encountering considerable toxicity.

CONCLUSION

Currently, graphene-based nanomaterials have numerous applications in the fields of tissue engineering, drug delivery, and regenerative medicine. In this study, at first, AgNWs/rGO composite was successfully synthesized and fabricated. Then, various spectroscopic techniques were employed to investigate the binding properties between AgNWs/rGO composite and HSA. The results displayed that AgNWs/rGO composite could form a complex with HSA. However, AgNWs/rGO composite did not induce alternation in the secondary structure of HSA. Furthermore, HSA maintained most of its activity in the presence of AgNWs/rGO composite. The MTT assay, DAPI staining, and flow cytometry analysis illustrated that AgNWs/rGO composite has no toxic effects in hEnSCs at lower concentrations. Thus, the results obtained from this study indicate that the prepared AgNWs/rGO composite, potentially, is suitable in nanomedicine applications such as tissue engineering and drug delivery.

ACKNOWLEDGMENTS

The authors thank Professor Gholamhossein Riazi (Institute of Biochemistry and Biophysics of Tehran University) for assistance with MTT assays.

REFERENCES

1.Shin SR, Li Y-C, Jang HL, Khoshakhlagh P, Akbari M, Nasajpour A, Zhang YS, Tamayol A, Khademhosseini A. Graphene-based materials for tissue engineering. Adv Drug Deliv Rev. 2016; 105: 255-274.

2.Roy I, Rana D, Sarkar G, Bhattacharyya A, Saha NR, Mondal S, Pattanayak S, Chattopadhyay S, Chattopadhyay D. Physical and electrochemical characterization of reduced graphene oxide/silver nanocomposites synthesized by adopting a green approach. RSC Adv. 2015; 5(32): 25357-25364.

3.Yang K, Feng L, Shi X, Liu Z. Nano-graphene in biomedicine: theranostic applications. Chem Soc Rev. 2013; 42(2): 530-547.

4.Chung C, Kim Y-K, Shin D, Ryoo S-R, Hong BH, Min D-H. Biomedical applications of graphene and graphene oxide. Acc Chem Res. 2013; 46(10): 2211-2224.

5.Hatamie S, Ahadian MM, Zomorod MS, Torabi S, Babaie A, Hosseinzadeh S, Soleimani M, Hatami N, Wei Z-H. Antibacterial properties of nanoporous graphene oxide/cobalt metal organic framework. Mater Sci Eng C. 2019; 104: 109862.

6.Hatamie S, Mohamadyar-Toupkanlou F, Mirzaei S, Ahadian MM, Hosseinzadeh S, Soleimani M, Sheu WJ, Wei ZH, Hsieh TF, Chang WC, Wang CL. Cellulose acetate/magnetic graphene nanofiber in enhanced human mesenchymal stem cells osteogenic differentiation under alternative current magnetic field. Spin. 2019; 9(2): 1940011.

7.Nazari H, Azadi S, Hatamie S, Zomorrod MS, Ashtari K, Soleimani M, Hosseinzadeh S. Fabrication of graphene-silver/polyurethane nanofibrous scaffolds for cardiac tissue engineering. Polym Adv Technol. 2019; 30(8): 2086-2099.

8.Hatamie S, Akhavan O, Sadrnezhaad SK, Ahadian MM, Shirolkar MM, Wang HQ. Curcumin-reduced graphene oxide sheets and their effects on human breast cancer cells. Mater Sci Eng C. 2015; 55: 482-489.

9.Yang K, Wan J, Zhang S, Zhang Y, Lee S, Liu Z. Long term biodistribution and toxicology of pegylated graphene in mice Parmacokinetic vivo, editor. ACS Nano. 2011; 5: 516-544.

10.He Y, Jiao B, Tang H. Interaction of single-stranded DNA with graphene oxide: fluorescence study and its application for S1 nuclease detection. RSC Adv. 2014; 4(35): 18294-18300.

11.Sun B, Zhang Y, Chen W, Wang K, Zhu L. Concentration dependent effects of bovine serum albumin on graphene oxide colloidal stability in aquatic environment. Environ Sci Technol. 2018; 52(13): 7212-7219.

12.Hekmat A, Saboury AA, Divsalar A. The effects of silver nanoparticles and doxorubicin combination on DNA structure and its antiproliferative effect against T47D and MCF7 cell lines. J Biomed Nanotechnol. 2012; 8(6): 968-982.
13.Xia Y, Yang P, Sun Y, Wu Y, Mayers B, Gates B, Yin Y, Kim F, Yan H. One-dimensional nanostructures: synthesis, characterization, and applications. Adv Mater. 2003; 15(5): 353-389.
14.Zhang Y, Xu J, Yang Y, Sun B, Wang K, Zhu L. Impacts of proteins on dissolution and sulfidation of silver nanowires in aquatic environment: Importance of surface charges. Environ Sci Technol. 2020; 54: 5560–5568.
15.Hekmat A, Salavati F, Tackallou SH. The Effects of Paclitaxel in the Combination of Diamond Nanoparticles on the Structure of Human Serum Albumin (HSA) and Their Antiproliferative Role on MDA-MB-231cells. Protein J. 2020; 39: 268-283.
16.Liu Z, Chen X. Simple bioconjugate chemistry serves great clinical advances: albumin as a versatile platform for diagnosis and precision therapy. Chem Soc Rev. 2016; 45(5): 1432-1456.
17.Purcell M, Neault JF, Tajmir-Riahi HA. Interaction of taxol with human serum albumin. Biochim Biophys Acta. 2000; 1478(1): 61-68.
18.Mohamadi F, Ebrahimi-Barough S, Nourani MR, Mansoori K, Salehi M, Alizadeh AA, Tavangar SM, Sefat F, Sharifi S, Ai J. Enhanced sciatic nerve regeneration by human endometrial stem cells in an electrospun poly (ε-caprolactone)/collagen/NBG nerve conduit in rat. Artif Cells Nanomed Biotechnol. 2018; 46(8): 1731-1743.
19.Mobarakeh ZT, Ai J, Yazdani F, Sorkhabadi SMR, Ghanbari Z, Javidan AN, Mortazavi-Tabatabaei SA, Massumi M, Barough SE. Human endometrial stem cells as a new source for programming to neural cells. Cell Biol Int Rep. 2012; 19(1): 7-14.
20.Zhang Y, Xu J, Yang Y, Sun B, Wang K, Zhu L. Impacts of Proteins on Dissolution and Sulfidation of Silver Nanowires in an Aquatic Environment: Importance of Surface Charges. Environ Sci Technol. 2020; 54(9): 5560-5568.
21.Zhang L, Zhu W, Huang Y, Qi S. Synergetic Effects of Silver Nanowires and Graphene Oxide on Thermal Conductivity of Epoxy Composites. Nanomaterials. 2019; 9(9): 1264.
22.Saini P, Sharma R, Chadha N. Determination of defect density, crystallite size and number of graphene layers in graphene analogues using X-ray diffraction and Raman spectroscopy. Indian J Pure Ap Phy. 2017; 55(9): 625-629.
23.Maurya N, Maurya JK, Singh UK, Dohare R, Zafaryab M, Moshahid Alam Rizvi M, Kumari M, Patel R. In vitro cytotoxicity and interaction of noscapine with human serum albumin: Effect on structure and esterase activity of HSA. Mol Pharm. 2019; 16(3): 952-966.
24.Tran QT, Huynh TMH, Tong DT, Nguyen ND. Synthesis and application of graphene–silver nanowires composite for ammonia gas sensing. Adv Nat Sci-Nanosci. 2013; 4(4): 045012.
25.Fallahi H, Azizi H, Ghasemi I, Karrabi M. Preparation and properties of electrically conductive, flexible and transparent silver nanowire/poly (lactic acid) nanocomposites. Org Electron. 2017; 44: 74-84.
26.Yousef S, Mohamed A, Tatariants M. Mass production of graphene nanosheets by multi-roll milling technique. Tribol Int. 2018; 121: 54-63.
27.Wang Y, Wang X, Wang J, Zhao Y, He W, Guo Z. Noncovalent interactions between a trinuclear monofunctional platinum complex and human serum albumin. Inorg Chem. 2011; 50(24): 12661-12668.
28.Amani N, Saberi MR, Khan Chamani J. Investigation by fluorescence spectroscopy, resonance rayleigh scattering and zeta potential approaches of the separate and simultaneous binding effect of paclitaxel and estradiol with human serum albumin. Protein Peptide Lett. 2011; 18(9): 935-951.
29.Chaves OA, Amorim APdO, Castro LH, Sant'Anna CMR, De Oliveira MC, Cesarin-Sobrinho D, et al. Fluorescence and docking studies of the interaction between human serum albumin and pheophytin. Molecules. 2015; 20(10): 19526-19539.
30.Nan Z, Hao C, Ye X, Feng Y, Sun R. Interaction of graphene oxide with bovine serum albumin: A fluorescence quenching study. Spectrochimica Acta A Mol Biomol Spectrosc. 2019; 210: 348-354.
31.Zhang H, Liu W, Yang L, Liu J, Wang Y, Mao X, Wang J, Xu X. Fabrication of Reduced Graphene Oxide-Ag Nanocomposites and Analysis on the Interaction with BSA. J Nanomater. 2019; 2019: 2707909.
32.Ranjbar S, Shokoohinia Y, Ghobadi S, Bijari N, Gholamzadeh S, Moradi N, Ashrafi-Kooshk MR, Aghaei A, Khodarahmi R. Studies of the interaction between isoimperatorin and human serum albumin by multispectroscopic method: identification of possible binding site of the compound using esterase activity of the protein. Sci World J. 2013; 2013: 305081.
33.Hekmat A, Saboury AA, Divsalar A, Seyedarabi A. Structural effects of TiO2 nanoparticles and doxorubicin on DNA and their antiproliferative roles in T47D and MCF7 cells. Anticancer Agents Med Chem. 2013; 13(6): 932-951.
34.Zhao X, Liu R, Chi Z, Teng Y, Qin P. New insights into the behavior of bovine serum albumin adsorbed onto carbon nanotubes: comprehensive spectroscopic studies. J Biomed Opt. 2010; 114(16): 5625-5631.
35.Masters B. Principles of Fluorescence Spectroscopy, Third Edition. J Biomed Opt. 2008; 13(2): 029901.
36.Lu Q, Chen C, Zhao S, Ge F, Liu D. Investigation of the interaction between gallic Acid and α-amylase by spectroscopy. Int J Food Prop. 2016; 19(11): 2481-2494.
37.Luo H, Song C, Lin X, Peng Z, Weng L, Tang X, Xu S, Song M, Jin L, Zheng X. Study on AgInZnS-graphene oxide non-toxic quantum dots for biomedical sensing. Front Chem. 2020; 8: 331.
38.Hekmat A, Hajebrahimi Z, Motamedzade A. Structural Changes of Human Serum Albumin (HSA) in Simulated Microgravity. Protein Peptide Lett. 2017; 24(11): 1030-1039.
39.Corrêa DH, Ramos CH. The use of circular dichroism spectroscopy to study protein folding, form and function. Afr J Biomed Res. 2009; 3(5): 164-173.
40.Fu X-B, Liu D-D, Lin Y, Hu W, Mao Z-W, Le X-Y. Water-soluble DNA minor groove binders as potential chemotherapeutic agents: synthesis, characterization, DNA binding and cleavage, antioxidation, cytotoxicity and HSA interactions. Dalton Trans. 2014; 43(23): 8721-8737.
41.Ghosh D, Dey SK, Saha C. Mutation induced conformational changes in genomic DNA from cancerous K562 cells influence drug-DNA binding modes. PLoS One. 2014; 9(1): e84880.
42.Sekowski S, Kazmierczak A, Mazur J, Przybyszewska M,

Zaborski M, Shcharbin D, Gabryelak T. The interaction between PAMAM G3. 5 dendrimer, Cd2+, dendrimer–Cd2+ complexes and human serum albumin. Colloids Surf B. 2009; 69(1): 95-98.

43.Kubiak-Ossowska K, Jachimska B, Mulheran PA. How negatively charged proteins adsorb to negatively charged surfaces: a molecular dynamics study of BSA adsorption on silica. J Phys Chem B. 2016; 120(40): 10463-10468.

44.Lehmann SG, Toybou D, del Real A-EP, Arndt D, Tagmount A, Viau M, Safi M, Pacureanu A, Cloetens P, Bohic S, Salomé M, Castillo-Michel H, Omaña-Sanz B, Hofmann A, Vulpe C, Simonato J-P, Celle C, Charlet L, Gilbert B. Crumpling of silver nanowires by endolysosomes strongly reduces toxicity. Proc Natl Acad Sci. 2019; 116(30): 14893-14898.

45.An HJ, Sarkheil M, Park HS, Yu IJ, Johari SA. Comparative toxicity of silver nanoparticles (AgNPs) and silver nanowires (AgNWs) on saltwater microcrustacean, Artemia salina. Comp Biochem Phys C. 2019; 218: 62-69.

46.Wang F, Wang Y, Qu G, Yao X, Ma C, Song M, Wang H, Jiang G. Ultralong AgNWs-induced toxicity in A549 cells and the important roles of ROS and autophagy. Ecotoxicol Environ Saf. 2019; 186: 109742.